

QC
807.5
•U66
no. 377

NOAA Technical Report ERL 377-APCL 39



A Three-Dimensional Simulation of Winds and Non-Precipitating Orographic Clouds Over Hawaii

Everett C. Nickerson
Elemer L. Magaziner

September 1976

U.S. DEPARTMENT OF COMMERCE
National Oceanic and Atmospheric Administration
Environmental Research Laboratories

QC
807.5
U66
No. 377

NOAA Technical Report ERL 377-APCL 39

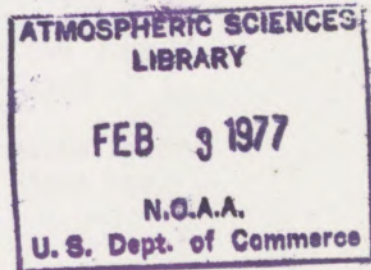


A Three-Dimensional Simulation of Winds and Non-Precipitating Orographic Clouds Over Hawaii

Everett C. Nickerson
Elemer L. Magaziner

Atmospheric Physics and Chemistry Laboratory
Boulder, Colorado

September 1976



U.S. DEPARTMENT OF COMMERCE

Elliot Richardson, Secretary

National Oceanic and Atmospheric Administration
Robert M. White, Administrator

Environmental Research Laboratories
Wilmot Hess, Director



Plates

- Plate 1. Photograph of a model of Hawaii at the City of Refuge National Historical Park, Hawaii. The color shading indicates the approximate distribution of vegetation and lava flows.
- Plate 2. Photograph of the windswept trees southwest of Waimea.
- Plate 3. Photograph of the Kohala cloud from a location southwest of Waimea.
- Plate 4. Photograph of Hawaii taken from Apollo 9. The NASA caption reads: "Here the island of Hawaii looks like a dark-visaged monster peering up out of the sea beyond the lunar module in the foreground. The snow-tufted peaks of Mauna Loa and Mauna Kea resemble eyes, and the wedge-shaped cloud bank where the trade wind was flowing over the saddle between those peaks suggests a brow. There are often moisture-laden clouds on the windward side of a high tropical island and scarcely any on the leeward side." Arrows A-A point to the summit of Mauna Kea; arrows B-B point to the summit of Mauna Loa.



Plate 1.



Plate 2.



Plate 3.

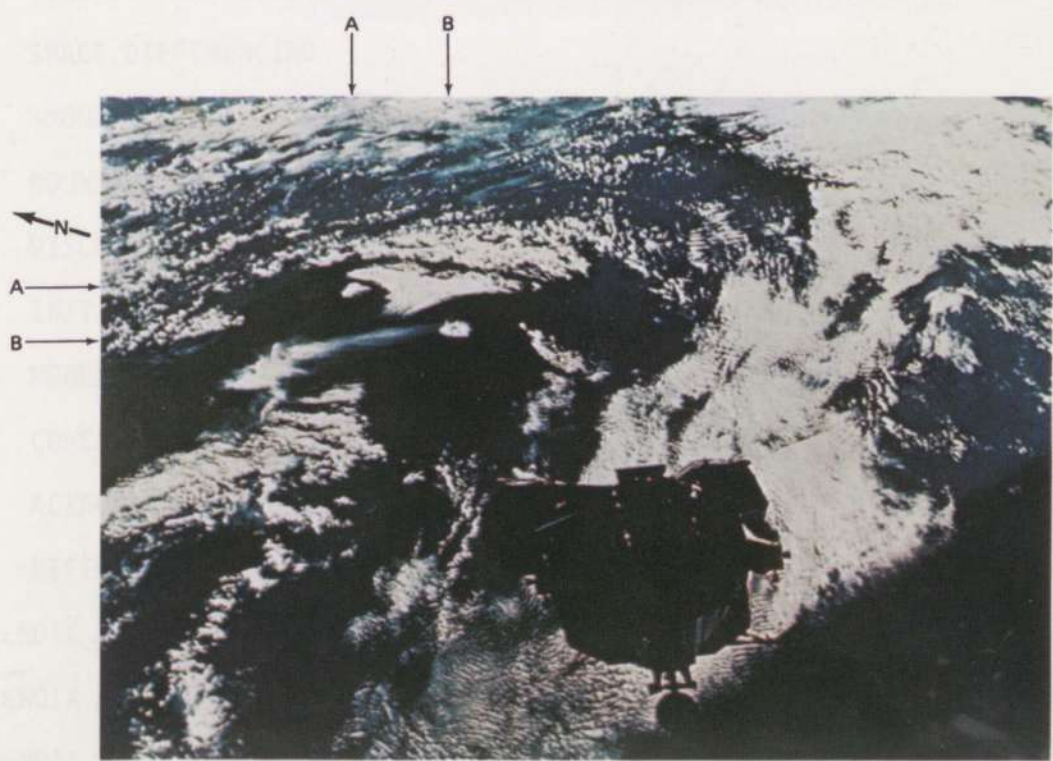


Plate 4.

CONTENTS

	Page
Plate 1	iv
Plate 2	iv
Plate 3	v
Plate 4	v
Abstract	1
1. INTRODUCTION	1
2. BASIC EQUATIONS	2
3. LOWER BOUNDARY CONDITIONS	5
4. PLANETARY BOUNDARY LAYER	7
5. VERTICAL GRID	9
6. HORIZONTAL GRID	10
7. TIME DIFFERENCING	11
8. SPACE DIFFERENCING	11
9. SMOOTHING OPERATOR	15
10. BOUNDARY CONDITIONS	15
11. DISCUSSION	15
12. INITIAL CONDITIONS	19
13. MODEL RESULTS	19
14. CONCLUSION	26
15. ACKNOWLEDGMENTS	27
16. REFERENCES	27
APPENDIX A. BASIC NOMENCLATURE	29
APPENDIX B. TERRAIN PARAMETERS	31
APPENDIX C. EXCERPT FROM U.S.W.B. CLIMATOLOGICAL SUMMARY	34

A THREE-DIMENSIONAL SIMULATION OF WINDS AND NON-PRECIPITATING OROGRAPHIC CLOUDS OVER HAWAII

Everett C. Nickerson
and
Elemer L. Magaziner

A mesoscale model is presented, designed with the capability of simulating moist, non-precipitating, three-dimensional flow over mountainous terrain. The model makes use of a transformed sigma coordinate system to assure adequate resolution in the boundary layer. A preliminary evaluation of the performance of the model has been obtained from simulations of airflow and orographically induced cloud cover over the island of Hawaii.

1. INTRODUCTION

Numerical models on an operational basis are now capable of reasonably accurate 48-hour forecasts of synoptic scale disturbances. However, those significant weather events that greatly affect our daily lives, such as heavy precipitation and damaging winds, are usually on a much smaller scale and therefore not directly resolvable by the large scale models. Detailed forecasts for specific areas make use of information contained in the fields of large scale convergence, flow patterns, moisture supply, and atmospheric stability as well as local climatological information. That is, synoptic scale predictions of wind, temperature, moisture, and pressure fields do not in themselves indicate the occurrence of severe weather in a given locality, but their structure may indicate to an experienced person the likelihood of such occurrences.

If you examine the status of current modeling efforts on the scale of individual convective clouds, you find that three-dimensional time dependent simulations are now possible. Many microphysical questions need to be resolved and sub-grid scale closure poses a difficult challenge; nevertheless, the numerical simulation of isolated convective clouds is technically feasible.

The fact that significant progress has been made in the numerical modeling of these two dissimilar scales of motion is not fortuitous but is rather a manifestation of the energetics that characterize atmospheric motions. Current evidence suggests the existence of a bimodal distribution in the atmospheric kinetic energy spectrum, with peaks roughly at 4 days and at 1 minute (see Fiedler and Panofsky, 1970). The first peak is associated with synoptic scale baroclinic disturbances and the second with convective activity.

Between these two peaks lies a broad minimum or "mesoscale gap." Strong controls on mesoscale systems are therefore exerted by the synoptic scale. These controls, manifesting themselves as time-dependent lateral boundary conditions for mesoscale models, also provide the forcing that leads to energy conversions on smaller scales. The specification of sub-grid scale processes is even more difficult for mesoscale than for synoptic scale motions since the percentage of area covered by active updrafts may not be as small as is presumed in some parameterization schemes. A mesoscale model must therefore provide realistically for larger scale forcing as well as for sub-grid scale convective transports of a rather general nature.

Significant progress in the modeling of mesoscale disturbances is essential for more accurate forecasts of the damaging aspects of severe storms. Mesoscale models are also needed for the planning and evaluation of future attempts to modify severe storms, since fiscal constraints would prohibit the gathering of statistically significant data.

Cumulus parameterization theory is being developed on a very sophisticated level for general circulation models, and yet the local recycling of mass and momentum by individual clouds is still not well understood. Despite the complexity of the problem, significant progress in developing a mesoscale model can still be made by formulating the basic equations to treat stable precipitation and other important physical processes. The details of a three-dimensional terrain model designed to simulate three-dimensional airflow over complex terrain are presented in sections 2 to 10 of this report. Preliminary results using the island of Hawaii as a test case are contained in sections 11 to 14.

2. BASIC EQUATIONS

In the presence of favorable synoptic scale conditions, the vertical fluxes of heat, momentum, and moisture within the atmospheric surface layer can exert a strong influence on the location, duration, and intensity of severe convective storms. Satellite pictures have clearly shown that pre-existing cloud cover can effectively suppress surface heating over a wide area and thereby prevent the development of convective activity (Weiss and Purdom, 1974). Moreover, variations in terrain, coupled with unevenness in surface heating, can produce slope winds, mountain-valley winds, and sea breeze circulation systems. A constant flux layer 100 m or more in depth is not at all uncommon during periods of strong insolation; however, the depth of that layer may decrease by an order of magnitude during nighttime hours.

In order to provide for increased vertical resolution at the lower boundary and still to retain the advantages of a uniform grid, the following coordinate transformation was incorporated into the model:

$$\sigma = (4v - v^4)/3 \quad (1)$$

where σ is the conventional normalized pressure coordinate.

The basic equations for the Nu coordinate system are as follows:

$$\frac{\partial U}{\partial t} = - \frac{\partial(Uu)}{\partial x} - \frac{\partial(Uv)}{\partial y} - \frac{1}{\sigma'} \frac{\partial(\sigma'U\dot{v})}{\partial v} + fV + \left(\phi - \frac{RT^* \sigma \pi}{P} \right) \frac{\partial \pi}{\partial x} - \frac{\partial(\pi\phi)}{\partial x} + F_U \quad (2)$$

$$\frac{\partial V}{\partial t} = - \frac{\partial(Vu)}{\partial x} - \frac{\partial(Vv)}{\partial y} - \frac{1}{\sigma'} \frac{\partial(\sigma'V\dot{v})}{\partial v} - fU + \left(\phi - \frac{RT^* \sigma \pi}{P} \right) \frac{\partial \pi}{\partial y} - \frac{\partial(\pi\phi)}{\partial y} + F_V \quad (3)$$

$$\frac{\partial S}{\partial t} = - \frac{\partial(Su)}{\partial x} - \frac{\partial(Sv)}{\partial y} - \frac{1}{\sigma'} \frac{\partial(\sigma'S\dot{v})}{\partial v} + \frac{\pi Q}{T} + F_S \quad (4)$$

$$\frac{\partial W}{\partial t} = - \frac{\partial(Wu)}{\partial x} - \frac{\partial(Wv)}{\partial y} - \frac{1}{\sigma'} \frac{\partial(\sigma'W\dot{v})}{\partial v} + F_W \quad (5)$$

$$\frac{\partial \pi}{\partial t} = - \int_0^1 \left(\frac{\partial U}{\partial x} + \frac{\partial V}{\partial y} \right) \sigma' dv \quad (6)$$

$$\dot{v} = - \frac{1}{\pi \sigma'} \int_0^V \sigma' \left(\frac{\partial \pi}{\partial t} + \frac{\partial U}{\partial x} + \frac{\partial V}{\partial y} \right) dv \quad (7)$$

$$\frac{\partial \phi}{\partial P} = - C_p \theta (1 + 0.61 q_v) \quad (8)$$

If P_s is the surface pressure and P_T is the pressure at the top of the model, then

$$\pi = P_s - P_T \quad (9)$$

and

$$\sigma = (P - P_T)/\pi \quad (10)$$

We also have made the following definitions (these supplement those in Appendix A):

$$U = \pi u \quad (11)$$

$$V = \pi v \quad (12)$$

$$\sigma' = d\sigma/dv \quad (13)$$

$$\dot{v} = dv/dt \quad (14)$$

$$\hat{p} = (P/p_0)^k \quad (15)$$

$$\phi = gz \quad (16)$$

$$T^* = T(1 + 0.61 q_v) \quad (17)$$

$$S = \pi(\ln(T/\hat{p}) + Lq_v/C_p T) \quad (18)$$

$$W = \pi(q_v + q_{cw}) \quad (19)$$

$$L = 597.3 - 0.566(T - 273.16) \quad (20)$$

Here q_v and q_{cw} represent the mixing ratio for water vapor and cloud water, respectively. For all calculations reported on in this paper, p_0 is 1013 mb, and p_T is zero.

Temperature is not explicitly predicted by the model, but must be extracted from the predicted value of the entropy variable, S . If the air is saturated, the mixing ratio is a known function of temperature, and (18) becomes a transcendental equation for the temperature, T_s corresponding to saturation with respect to liquid water. If on the other hand the air is unsaturated, the mixing ratio in (18) is replaced by W/π and the temperature is solved for directly, using the temperature at the previous time step to account for the temperature dependence of the latent heat. In the present formulation of the model no conversion of cloud water to precipitation is included, and saturation with respect to liquid water is required for any cloud water to be present.

In order to determine the temperature and moisture variables, we first compute T_s and q_{vs} , the saturation temperature and its corresponding mixing ratio (the Newton-Raphson technique is currently being used). Temperature and mixing ratio are then arrived at in accordance with the following criteria:

$$\left. \begin{array}{l} q_v = q_{vs} \\ q_{cw} = W/\pi - q_{vs} \\ T = T_s \end{array} \right\} \quad W > \pi q_{vs},$$

$$\left. \begin{array}{l} q_v = W/\pi \\ q_{cw} = 0 \\ T = T_{uns} \end{array} \right\} \quad W \leq \pi q_{vs} .$$

The saturation vapor pressure with respect to water, e_s , used to compute q_{vs} is taken from Murray (1967),

$$e_s = 6.11 \exp [17.27(T-273.16)/(T-35.86)] . \quad (21)$$

3. LOWER BOUNDARY CONDITIONS

A constant flux layer is presumed to exist between the lower boundary (with roughness length z_0), and the first grid point above the surface, $z = h$. The friction velocity and surface fluxes of sensible and latent heat are computed using the Bussinger-Dyer surface layer formulation (see Nickerson and Smiley, 1975).

$$\frac{u}{u^*} = F \left(\frac{z}{L}, \frac{z}{z_0} \right) \quad (22)$$

$$\frac{(\theta - \theta_0) u^*}{-w' \theta_0} = G \left(\frac{z}{L}, \frac{z}{z_0} \right) , \quad (23)$$

where L is the Monin-Obukhov length, and where the functional forms for F and G depend on the density stratification.

In order to link the theoretical formulation with the discretization scheme used in the model it is convenient to define a bulk Richardson number for the surface layer,

$$R_{iB} = \frac{hg(\theta_h - \theta_0)}{\theta_h u_h^2} , \quad (24)$$

where the subscript h denotes the value at the height h .

If we now set

$$L = \frac{-u_*^3 \theta_h}{kg \overline{w' \theta_0}} , \quad (25)$$

(25) may be rewritten in the form

$$F(z/L) = Gz/L - k F^2 R_{i_B} = 0 . \quad (26)$$

For a given value of bulk Richardson number and surface roughness, (26) becomes a transcendental equation for z/L , where z is now h . After solving (26) for h/L , we then have

$$u_* = u_h/F \quad (27)$$

$$\overline{w' \theta_0} = u_h(\theta_0 - \theta_h)/FG , \quad (28)$$

$$\overline{w' q_0} = u_h(q_0 - q_h)/FG . \quad (29)$$

For unstable conditions (i.e., $\theta_0 - \theta_h > 0$), the functions F and G have the form

$$kF = \ell n \left[\frac{(\zeta-1)(\zeta_0+1)}{(\zeta+1)(\zeta_0-1)} \right] + 2 \tan^{-1} \zeta - 2 \tan^{-1} \zeta_0 \quad (30)$$

$$kG = R \ell n \left[\frac{(n^2-1)(n_0^2+1)}{(n^2+1)(n_0^2-1)} \right] , \quad (31)$$

where

$$\zeta = (1 - \gamma z/L)^{1/4}, \quad (32)$$

$$\zeta_0 = (1 - \gamma z_0/L)^{1/4}, \quad (33)$$

$$\eta = (1 - \gamma'' z/L)^{1/4}, \quad (34)$$

$$\eta_0 = (1 - \gamma'' z_0/L)^{1/4}, \quad (35)$$

For mildly stable conditions (i.e., $z/L < 1$), the functions F and G have the form

$$kF = \ell n (z/z_0) + \beta z/L, \quad (36)$$

$$kG = R \ell n (z/z_0) + \beta z/L. \quad (37)$$

For $z/L > 1$, the functions F and G are obtained from profiles given by Webb (1970).

$$kF = \beta \ell n (z/L) + \ell n (z/z_0) + \beta \quad (38)$$

$$kG = (1 + \beta - R) \ell n (z/L) + R \ell n (z/z_0) + \beta. \quad (39)$$

At the present stage of model development the surface temperature and mixing ratio are specified initially and not allowed to change during the course of the model run.

4. PLANETARY BOUNDARY LAYER

A boundary layer is presumed to exist between z_B , the first grid point above the surface and z_A , some specified height where the winds become decoupled from surface layer effects. At the present time z_A is set equal to one kilometer. Exchange coefficients for momentum, $K(u)$, and for the temperature and moisture, $K(T)$, between z_A and z_B are computed in accordance with the profile given by O'Brien (1970).

$$K = K_A + \left[(z - z_A) / (\Delta z)^2 \right] \left[K_B - K_A + (z - z_B)(K'_B + 2(K_B - K_A) / \Delta z) \right] \quad (40)$$

The prime denotes a derivative with respect to z , and $\Delta z = (z_A - z_B)$. Both $K(u)$ and $K(T)$ are set equal to zero for heights greater than z_A . Moreover, horizontal friction is not explicitly included in the model except at the top and on the lateral boundaries (see section 10).

The frictional terms in (2), (3), (4), and (5) are written as

$$F_u = A \frac{\partial}{\partial v} \left(AK(u) \frac{\partial U}{\partial v} \right) \quad (41)$$

$$F_v = A \frac{\partial}{\partial v} \left(AK(U) \frac{\partial V}{\partial v} \right) \quad (42)$$

$$F_s = A \frac{\partial}{\partial v} \left(AK(T) \frac{\partial S}{\partial v} \right) \quad (43)$$

$$F_w = A \frac{\partial}{\partial v} \left(AK(T) \frac{\partial W}{\partial v} \right) , \quad (44)$$

where $A = \frac{-gp}{RT\pi\sigma}$.

At the lower boundary ($v = \sigma = 1$),

$$AK(u) \frac{\partial U}{\partial v} = \pi u_*^2 \cos \alpha \quad (45)$$

$$AK(u) \frac{\partial V}{\partial v} = \pi u_*^2 \sin \alpha \quad (46)$$

$$AK(T) \frac{\partial S}{\partial v} = \pi \left(\frac{Q_S \hat{P}}{T} + \frac{LQ_e}{C_p} \right) \quad (46)$$

$$AK(T) \frac{\partial W}{\partial v} = \pi Q_e \quad (48)$$

where $\tan \alpha = V_h/U_h$, the ratio of the two wind components at the first grid point above the surface, and where

$$\pi Q_s = (\theta_0 - \theta_h) \sqrt{U_h^2 + V_h^2} / FG \quad (49)$$

$$\pi Q_e = (q_0 - q_h) \sqrt{U_h^2 + V_h^2} / FG \quad (50)$$

5. VERTICAL GRID

The vertical grid consists of 15 equally spaced levels in the Nu coordinate system. With reference to Figure 1, the variable ν is defined at the circled levels, and all other variables are defined at the crosses.

Vertical distances in the Nu coordinate system range from zero to unity, just as in the sigma system. Furthermore, equation (1) satisfies the condition noted by De Rivas (1972), that $d\sigma/d\nu$ must be finite over the entire domain and must be equal to zero at $\nu = \sigma = 1$ in order to assure second order accuracy in the discretization scheme. The vertical grid corresponding to the 15 levels in the model is shown in Table 1, together with the corresponding sigma levels. The first grid point is located approximately 18 meters above the lower boundary.

Table 1. Comparison of the Two Coordinate Systems' Vertical Grids

ν	σ
0.0000	0.0000
0.0333	0.0444
0.1000	0.1333
0.1667	0.2220
0.2333	0.3101
0.3000	0.3973
0.3667	0.4829
0.4333	0.5660
0.5000	0.6458
0.5667	0.7212
0.6333	0.7908
0.7000	0.8533
0.7667	0.9071
0.8333	0.9504
0.9000	0.9813
0.9667	0.9978
1.0000	1.0000

6. HORIZONTAL GRID

A staggered grid (fig. 2) is used to reduce the truncation errors on the level Nu surfaces (see Anthes and Warner, 1974). The variables u and v are defined at the crosses, while all thermodynamic variables are defined at the dots. The variable \dot{v} is not defined on this horizontal level but at distances $\Delta\nu/2$ above or below this level and at positions corresponding to the dots. For the runs reported on in this paper, Δx and Δy have both been set equal to 10 km. With 26 grid points in each direction, this corresponds to an area 250 km on a side.

	Grid Level	Condition on Nu $\nu=0$
x	1	
o		
x	2	
o		
x	3	
o		
x	4	
*		
*		
*		
x	13	
o		
x	14	$\Delta\nu=1/15$
o		
x	15	$\nu=1$

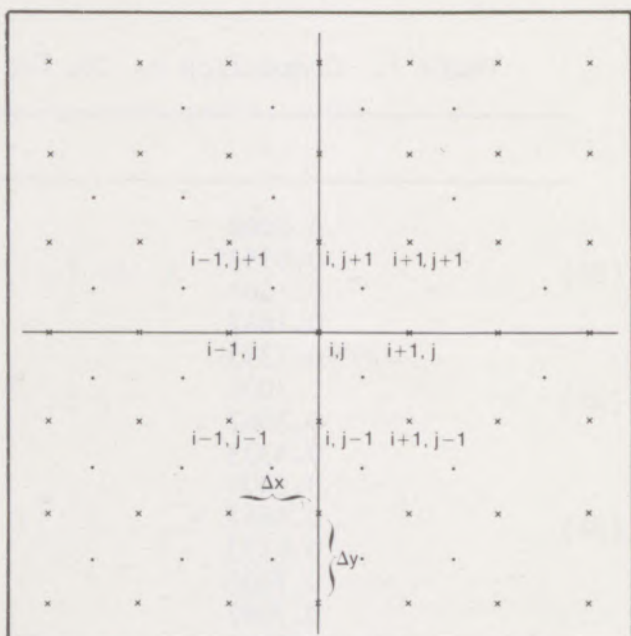


Figure 1. Vertical grid used in the model calculations.

Figure 2. Horizontal grid used in the model calculations.

7. TIME DIFFERENCING

Centered differences are used to represent the time derivative, except that every fifth time-step a Time and Space Uncentered Matsuno procedure is introduced (see Arakawa and Mintz, 1974). If, for example, we are dealing with the equation

$$\frac{dA}{dt} = F, \quad (51)$$

then the TASU - Matsuno scheme is as follows:

	<u>Time</u>	<u>Space</u>
$\frac{A^{*(n+1)} - A^n}{\Delta t} = F_c(A^n)$	Forward	Centered
$\frac{A^{n+1} - A^n}{\Delta t} = F_{ur}(A^{*(n+1)})$	Backward	Upper-Right
$\frac{A^{*(n+2)} - A^{n+1}}{\Delta t} = F_c(A^{n+1})$	Forward	Centered
$\frac{A^{n+2} - A^{n+1}}{\Delta t} = F_{11}(A^{*(n+2)})$	Backward	Lower-Left

8. SPACE DIFFERENCING

The horizontal grid and the discretization scheme that follows are based on Anthes and Warner (1974). The staggered grid has a smaller truncation error than a non-staggered grid. Perhaps more important, however, is the fact that boundary values of the velocity components appear only in the flux terms of the momentum equations and not in calculations using the continuity equation.

The finite difference analogs of equations (2) to (8) are

$$\left(\frac{\partial U}{\partial t} \right)_{i,j,k} = D_1(U) + D_2(U) + D_3(U) + fV + D_6(U) \quad (52)$$

$$\left(\frac{\partial V}{\partial t}\right)_{i,j,k} = D_1(V) + D_2(V) + D_3(V) - fU + D_7(V) \quad (53)$$

$$\left(\frac{\partial S}{\partial t}\right)_{i+\frac{1}{2}, j+\frac{1}{2}, k} = D_2(S) + D_4(S) + D_5(S) \quad (54)$$

$$\left(\frac{\partial W}{\partial t}\right)_{i+\frac{1}{2}, j+\frac{1}{2}, k} = D_2(W) + D_4(W) + D_5(W) \quad (55)$$

$$\left(\frac{\partial \pi}{\partial t}\right)_{i+\frac{1}{2}, j+\frac{1}{2}} = - \Delta v \sum_{k=1}^{15} \sigma' [D_8(U) + D_9(V)] \quad (56)$$

$$(\dot{v} \sigma' \pi)_{i+\frac{1}{2}, j+\frac{1}{2}, k-\frac{1}{2}} = - \Delta v \sum_{k'=1}^k \sigma' \left[\frac{\partial \pi}{\partial t} + D_8(U) + D_9(V) \right] \quad (57)$$

$$\phi_{i+\frac{1}{2}, j+\frac{1}{2}, k} = \phi_{i+\frac{1}{2}, j+\frac{1}{2}, k+1} + C_p \left[\theta_{k+\frac{1}{2}} (1 + 0.61 q_v)_{k+\frac{1}{2}} \left(\hat{P}_{k+1} - \hat{P}_k \right)_{i+\frac{1}{2}, j+\frac{1}{2}} \right] \quad (58)$$

where the following definitions have been made:

$$\begin{aligned} D_1(\lambda) &= - \frac{1}{4\Delta x} \left[(u_{i+1,j} + u_{i,j}) (\bar{\lambda}_{i+\frac{1}{2}, j+\frac{1}{2}} + \bar{\lambda}_{i+\frac{1}{2}, j-\frac{1}{2}}) \right. \\ &\quad \left. - (u_{i,j} + u_{i-1,j}) (\bar{\lambda}_{i-\frac{1}{2}, j+\frac{1}{2}} + \bar{\lambda}_{i-\frac{1}{2}, j-\frac{1}{2}}) \right] \\ &\quad - \frac{1}{4\Delta y} \left[(v_{i,j+1} + v_{i,j}) (\bar{\lambda}_{i+\frac{1}{2}, j+\frac{1}{2}} + \bar{\lambda}_{i-\frac{1}{2}, j+\frac{1}{2}}) \right. \\ &\quad \left. - (v_{i,j} + v_{i,j-1}) (\bar{\lambda}_{i+\frac{1}{2}, j-\frac{1}{2}} + \bar{\lambda}_{i-\frac{1}{2}, j-\frac{1}{2}}) \right] \end{aligned}$$

$$D_2(\lambda) = \frac{1}{\sigma' \Delta v} \left[(\dot{v} \sigma' \lambda)_{k+\frac{1}{2}} - (\dot{v} \sigma' \lambda)_{k-\frac{1}{2}} \right]$$

$$D_3(\lambda) = \frac{\bar{A}_{i,j,k}}{(\Delta v)^2} \left[(\lambda_{k+1} - \lambda_k)(\bar{A}K(u))_{k+\frac{1}{2}} - (\lambda_k - \lambda_{k-1})(\bar{A}K(u))_{k-\frac{1}{2}} \right]$$

$$D_4(\lambda) = -\frac{1}{4\Delta x} \left[(U_{i+1,j+1} + U_{i+1,j})(\lambda_{i+3/2,j+\frac{1}{2}} + \lambda_{i+\frac{1}{2},j+\frac{1}{2}}) \right.$$

$$\begin{aligned} & - (U_{i,j+1} + U_{i,j})(\lambda_{i+\frac{1}{2},j+\frac{1}{2}} + \lambda_{i-\frac{1}{2},j+\frac{1}{2}}) \\ & - \frac{1}{4\Delta y} \left[(V_{i+1,j+1} + V_{i,j+1})(\lambda_{i+\frac{1}{2},j+3/2} + \lambda_{i+\frac{1}{2},j+\frac{1}{2}}) \right. \\ & \left. - (V_{i+1,j} + V_{i,j})(\lambda_{i+\frac{1}{2},j+\frac{1}{2}} + \lambda_{i+\frac{1}{2},j-\frac{1}{2}}) \right] \end{aligned}$$

$$D_5(\lambda) = \frac{A_k}{(\Delta v)^2} \left[(\lambda_{k+1} - \lambda_k)(AK(T))_{k+\frac{1}{2}} - (\lambda_k - \lambda_{k-1})(AK(T))_{k-\frac{1}{2}} \right]$$

$$D_6(U) = \frac{\bar{C}}{2\Delta x} \left[\pi_{i+\frac{1}{2},j+\frac{1}{2}} - \pi_{i-\frac{1}{2},j+\frac{1}{2}} + \pi_{i+\frac{1}{2},j-\frac{1}{2}} - \pi_{i-\frac{1}{2},j-\frac{1}{2}} \right]$$

$$- \frac{1}{2\Delta x} \left[(\pi_\phi)_{i+\frac{1}{2},j+\frac{1}{2}} - (\pi_\phi)_{i-\frac{1}{2},j+\frac{1}{2}} + (\pi_\phi)_{i+\frac{1}{2},j-\frac{1}{2}} \right.$$

$$\left. - (\pi_\phi)_{i-\frac{1}{2},j-\frac{1}{2}} \right]$$

$$D_7(V) = \frac{\bar{C}}{2\Delta y} \left[\pi_{i+\frac{1}{2},j+\frac{1}{2}} - \pi_{i+\frac{1}{2},j-\frac{1}{2}} + \pi_{i-\frac{1}{2},j+\frac{1}{2}} - \pi_{i-\frac{1}{2},j-\frac{1}{2}} \right]$$

$$- \frac{1}{2\Delta y} \left[(\pi_\phi)_{i+\frac{1}{2},j+\frac{1}{2}} - (\pi_\phi)_{i+\frac{1}{2},j-\frac{1}{2}} + (\pi_\phi)_{i-\frac{1}{2},j+\frac{1}{2}} - (\pi_\phi)_{i-\frac{1}{2},j-\frac{1}{2}} \right]$$

$$D_8(U) = \frac{1}{2\Delta x} \left[U_{i+1,j+1} - U_{i,j+1} + U_{i+1,j} - U_{i,j} \right]$$

$$D_9(V) = \frac{1}{2\Delta y} \left[V_{i+1,j+1} - V_{i+1,j} + V_{i,j+1} - V_{i,j} \right]$$

$$U = \bar{\pi} u$$

$$V = \bar{\pi} v$$

$$\lambda_{k+\frac{1}{2}} = \frac{1}{2} (\lambda_k + \lambda_{k+1})$$

$$\bar{\lambda}_{i+\frac{1}{2}, j+\frac{1}{2}} = \frac{1}{4} (\lambda_{i+1,j+1} + \lambda_{i+1,j} + \lambda_{i,j+1} + \lambda_{i,j})$$

$$C = \phi - RT^* \sigma \pi / P$$

The vertical velocity, dz/dt , is also calculated in order to assist in the interpretation of the results. This is especially important for computations above steep mountain slopes where the usual approximation $w = -\omega/\rho g$ can even give the wrong sign. The vertical velocity is given by

$$w_{i+\frac{1}{2}, j+\frac{1}{2}, k} = \frac{1}{g} \left[\left(\frac{\phi^n - \phi^{n-1}}{\Delta t} \right)_{i+\frac{1}{2}, j+\frac{1}{2}, k} \right.$$

$$+ \frac{(\phi_{i+3/2, j+\frac{1}{2}} - \phi_{i-\frac{1}{2}, j+\frac{1}{2}})k}{2\Delta x} \bar{u}_{i+\frac{1}{2}, j+\frac{1}{2}, k}$$

$$+ \frac{(\phi_{i+\frac{1}{2}, j+3/2} - \phi_{i+\frac{1}{2}, j-\frac{1}{2}})k}{2\Delta y} \bar{v}_{i+\frac{1}{2}, j+\frac{1}{2}, k}$$

$$- \left(\frac{RT^* \pi \sigma'}{2P} \right)_k (\dot{v}_{k+\frac{1}{2}} + \dot{v}_{k-\frac{1}{2}})_{i+\frac{1}{2}, j+\frac{1}{2}} \right]$$

9. SMOOTHING OPERATOR

In order to suppress $2\Delta x$ noise in the flow fields, a smoother (see Shapiro, 1970) is applied to the predicted fields of πu , and πv .

A smooth value of a variable, λ , is defined by:

$$\tilde{\lambda} = \frac{1}{8} (\lambda_{i+1,j+1} + \lambda_{i-1,j+1} + \lambda_{i+1,j-1} + \lambda_{i-1,j-1} + 4 \lambda_{i,j})$$

10. BOUNDARY CONDITIONS

At the upper boundary ($\sigma = v = 0$), \dot{v} is set to zero. This is a reasonable condition when $P_T = 0$, but may lead to difficulties when P_T is greater than 100 mb. Quantities such as wind and temperature are set equal to values at the grid point immediately below the top of the model. Actual values chosen are not of great importance, however, since the equations are written in flux form (i.e. $\dot{v}\pi u$) and the terms containing boundary values vanish on the upper boundary due to the condition on \dot{v} .

The thermodynamic variables are specified at all boundaries. Winds are specified on inflow boundaries and extrapolated from interior values on outflow boundaries. In addition, a viscous term is added to the predictive equations for U and V on the lateral and top boundaries. This is applied only at the first two interior grid points and is a simple Laplacian operator evaluated at the (n-1) time level.

11. DISCUSSION

Model validation is an important part of any model development program. Before a model can be accepted as a useful operational or research tool, it must first be demonstrated that the model is capable of simulating significant features of the prototype data. The selection of a validation site is an especially important step in the evaluation of a complex meteorological model, because a site with well-defined patterns in the winds, precipitation, and cloud cover can provide many opportunities for comparison between model results and prototype data. The more features that a model is able to reproduce, the greater the confidence that can be placed in calculations for locations lacking a good data base. Moreover, in view of the numerous options available to the numerical modeler, such a site can also assist in the formulation and specification of computational boundary conditions, smoothing operators, and sub-gridscale parameterizations.

Within this context, the island of Hawaii (Plate 1, Figs. 3-4) appears to be an ideal prototype for a mesoscale model development program. The

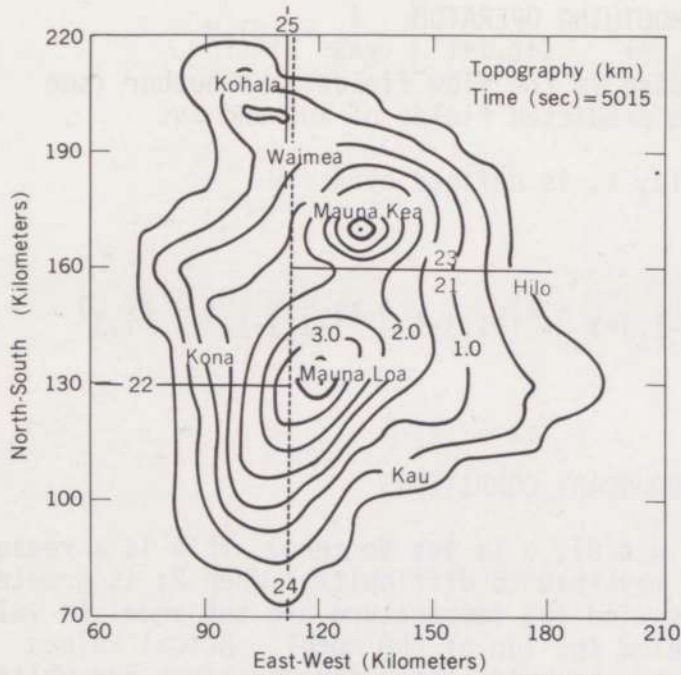


Figure 3. Elevation isopleths for Hawaii. Contour lines were drawn using linear interpolation between the values given in Appendix B. This figure also shows the locations of the vertical cross sections corresponding to figures 19-23.

relatively smooth topography, extending from sea level to 4.2 km, is characterized by barren lava fields, dry grasslands, rolling fields of sugar cane, and tropical rain forests. Considerable data have been gathered on rainfall and other meteorological parameters during Project Shower (Mordy et al., 1957), and also during the Warm Rain Project (Lavoie, 1966, and Lavoie et al., 1967). Part of a concise introduction to the meteorology of the island (NOAA, 1972) is reproduced in Appendix C.

The importance of the twin peaks Mauna Loa and Mauna Kea to the island meteorology cannot be overemphasized. Leeward convergence of the anti-cyclonic flow south of Mauna Loa and the cyclonic flow north of Mauna Kea results in a suppression of the vortex streets commonly observed in the cloud patterns downwind of tall islands. This zone of horizontal convergence (see Fig. 5, taken from Patzert, 1970) apparently interacts with the sea breeze to produce a secondary rainfall maximum on the leeward (Kona) coast (Chopra, 1973). The Kona rainfall maximum and the sharp demarcation between wet and dry areas are vividly illustrated in Fig. 6, which shows Lavoie's (1966)

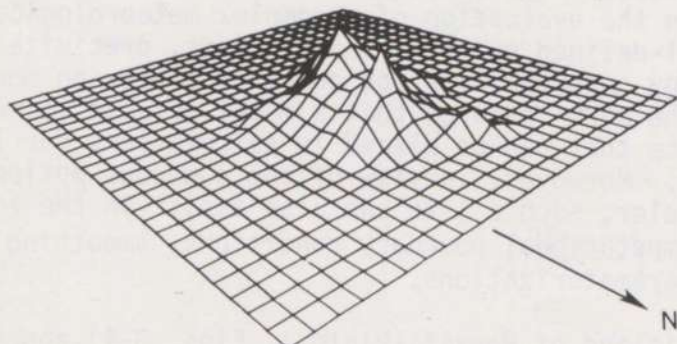


Figure 4. Terrain perspective of Hawaii. Locations of individual grid points coincide with the intersections of north-south and east-west lines. The view is from northeast (50°) looking southwest.



Figure 5. Composite surface wind field over Hawaiian waters taken from unpublished Weather Bureau Data, Honolulu (1968), after Patzert (1970).

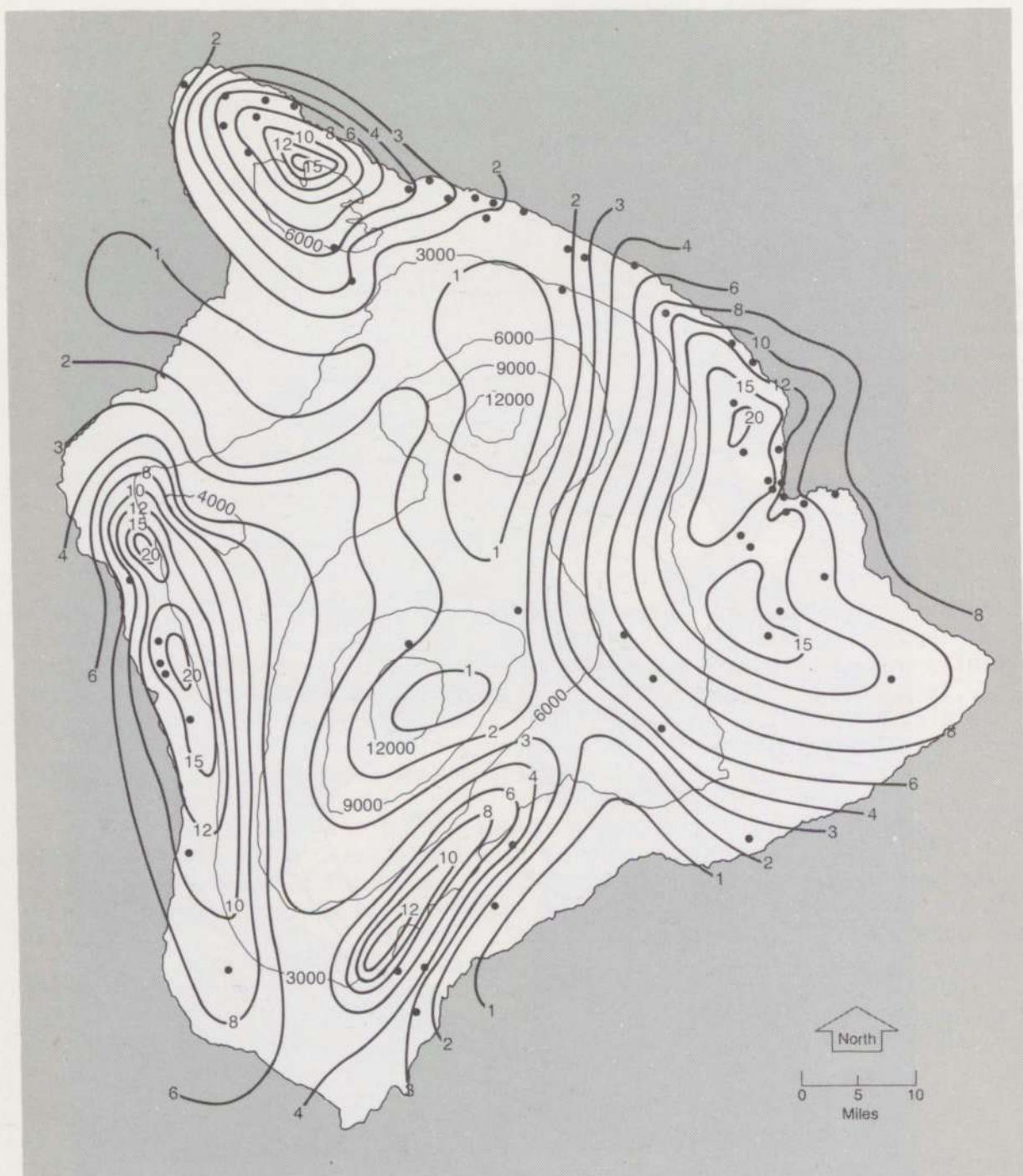


Figure 6. Rainfall for the period 11 July to 24 August 1965 from Lavoie (1966). Isohyets are labeled in inches.

summer rainfall distribution. Despite the occurrence of different wind regimes associated with winter storm systems, the locations of the precipitation maxima and minima in Fig. 6 also coincide with those of the annual pattern.

12. INITIAL CONDITIONS

During the fully developed and undisturbed trade wind regime, the air in the lowest few kilometers of the Eastern Pacific high has ample time to adjust to conditions at the ocean surface before encountering land. Under those conditions, topographical features or other sources of horizontal variability outside the computational domain ought to have little influence on the island weather. Representative inflow boundary data could therefore be obtained from an undisturbed trade wind sounding. The sounding station at Lihue, Kauai would probably provide the most representative data on a routine basis.

Initial conditions of wind, temperature, and mixing ratio for the numerical calculations are shown in Figs. 7, 8, and 9. The initial wind field contains easterlies at low levels and westerlies aloft. The temperature at the lower boundary remains constant in time, and decreases linearly with altitude from its sea level value of 299°K (see Fig. 10).

The temperature at the lower boundary has not been related to land use or vegetation; however, limited use of that information has been made in specifying the roughness length and mixing ratio at the surface. Vegetation and soil conditions were estimated from U.S.G.S. woodland print topographic charts. Roughness lengths were then obtained from Priestley (1959), Sellers (1966), and Sutton (1953). Terrain heights for individual grid points together with the corresponding surface parameters are listed in Appendix B.

13. MODEL RESULTS

All model results reported in this section were calculated in a terrain-following coordinate system. However, it is often more convenient to display the data using height as the vertical coordinate. Since the height of each grid point is known, the value of a quantity at some intermediate location is calculated using linear interpolation between two computational levels.

Horizontal windfields corresponding to elevations of 100, 1000, 1500, 2500, and 4000 meters above sea level are shown in Figs. 11-15. The low level convergence zone on the left side of Fig. 11 is of particular interest, and an expanded view of the convergence zone is shown in Fig. 16. Although the computed winds do not contain all the details of the composite wind field shown in Fig. 5, the model did succeed in reproducing some of the primary features including the leeward convergence zone.

The numerical computations indicate that the effects of the island on the airflow may be felt 50 to 100 km from land. A more accurate determination of the island influence region would require the calculations to be performed over a larger horizontal domain.

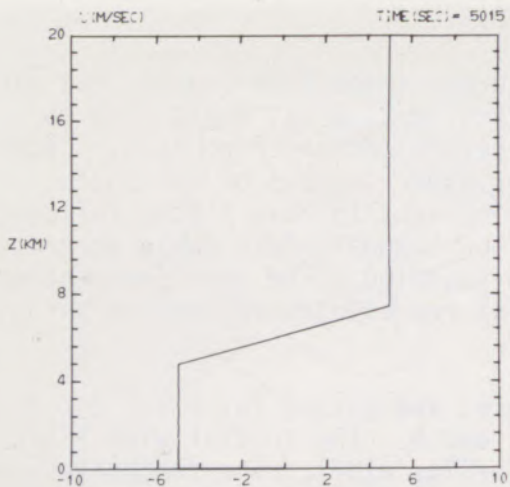


Figure 7. Initial wind profile over open water. V is initially zero everywhere, and both components are set equal to zero at the island surface.

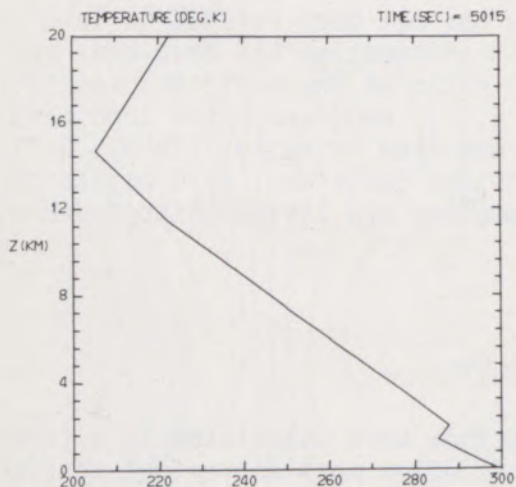


Figure 8. Initial temperature sounding over open water. Soundings over land begin at the elevations contained in Table B3 in accordance with the surface temperature distribution shown in Fig. 10.

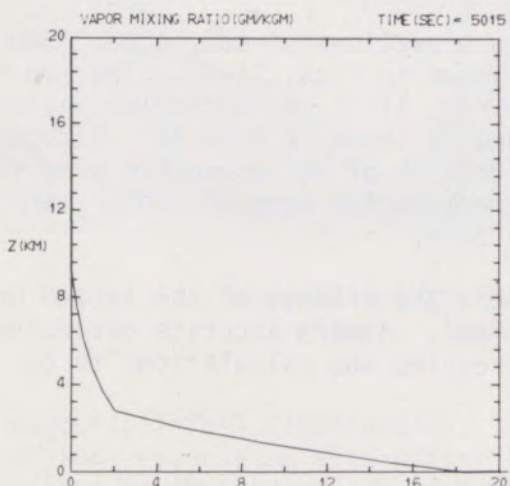
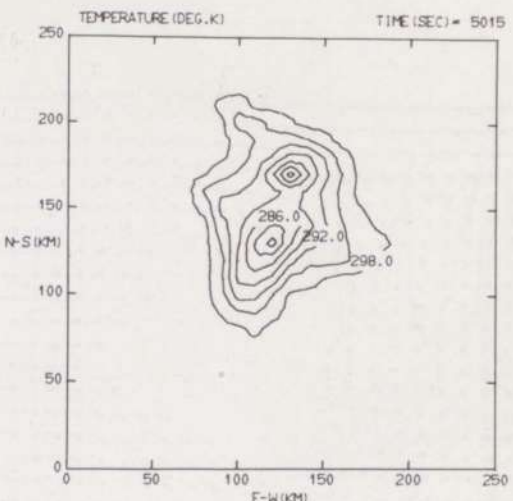


Figure 9. Initial mixing ratio sounding. The mixing ratio at the island surface is determined from the relative humidities given in Appendix B.

Figure 10. Isotherms along the island surface.



For the particular set of initial conditions used, Fig. 17 indicates that the strongest surface winds are located near the summit of Mauna Kea. At lower elevations, the area of strongest surface winds is along the north shore area and in the saddle region between Mauna Kea and the Kohala mountains (hereafter called the Kohala saddle). The asymmetry in the wind field is very apparent to the casual observer of Hawaiian weather. With the possible exception of some promontories, nowhere along the entire main highway that circles the island is one more aware of the presence of persistent strong winds than in the region just south of Waimea (the leeward edge of the Kohala saddle). Strong winds may occur at other locations but the trees of that area vividly portray their struggle for survival in the face of the persistent and forceful northeasterlies (see Plate 2).

Primary regions of convergence and divergence are quite apparent in the horizontal wind fields shown in Figs. 11-15. And yet there must be other, more subtle horizontal convergence patterns responsible for the extreme variability in the precipitation distribution of Fig. 6. Those terrain-induced regions of horizontal convergence become much more obvious when we examine the vertical motion field at an elevation of 1000 m above sea level as shown in Figs. 18a,b,c. An examination of Fig. 6 shows that all the major precipitation maxima are well correlated with the areas of rising motion in Figure 18a. Areas of strong descent in Fig. 18b also have their counterparts in the precipitation minima of Fig. 6. The Kau and South Kohala desert areas in particular are under the influence of sinking air, although the model calculations seem to have the North Kona rising motion intruding upon the South Kohala desert. The orographically forced upward motion on the windward slopes is relatively shallow (see Fig. 19), but in Fig. 20 we see that the leeward convergence zone is associated with a broad area of gradual ascent.

The correlation between the vertical motion field and observed precipitation does not carry over to the calculated cloud cover distribution nearly as well. A vertical cross section through the Mauna Loa-Mauna Kea saddle cloud (Fig. 21) shows a cloud only half the thickness of that observed by

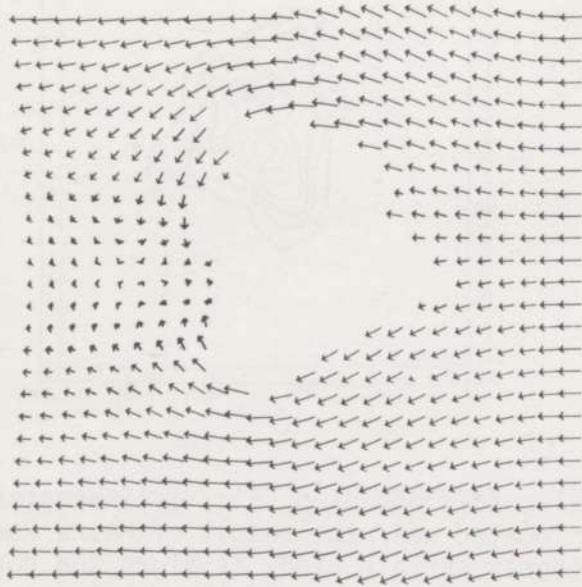


Figure 11. Vector wind field 100 m above sea level after 5015 s of model time. See Fig. 16 for an expanded view of the shaded area.

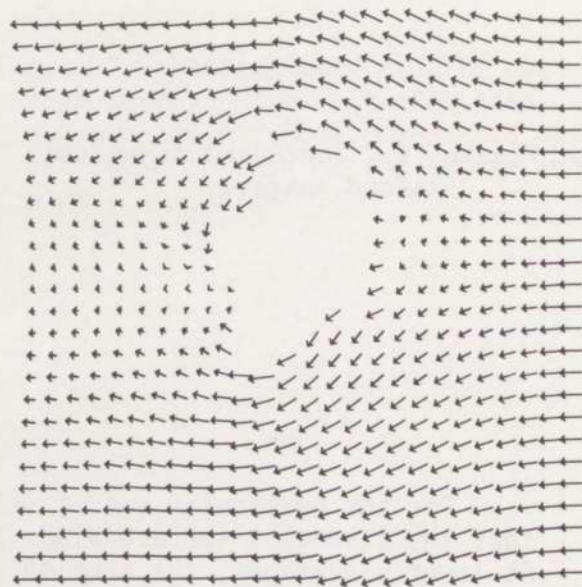


Figure 12. Vector wind field at 1000 m above sea level after 5015 s of model time.

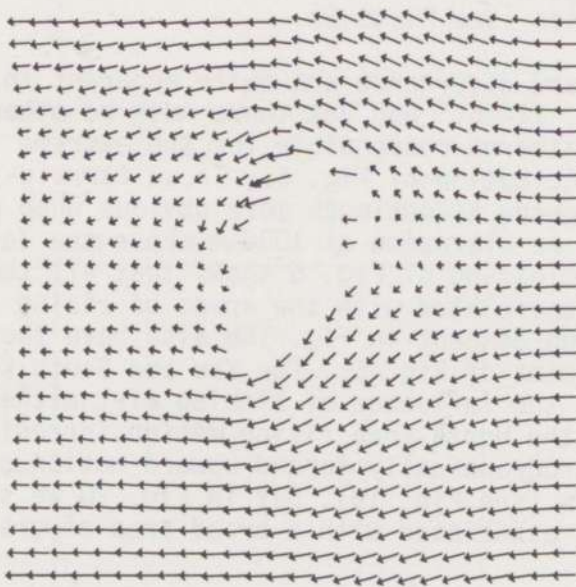


Figure 13. Vector wind field at 1500 m above sea level after 5015 s of model time.

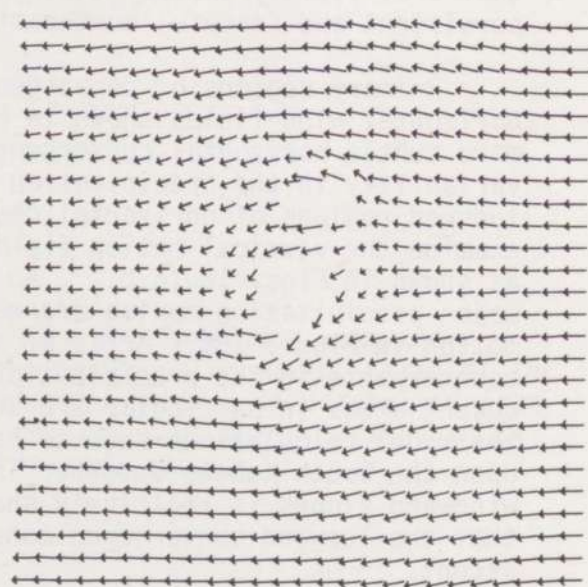


Figure 14. Vector wind field at 2500 m above sea level after 5015 s of model time.

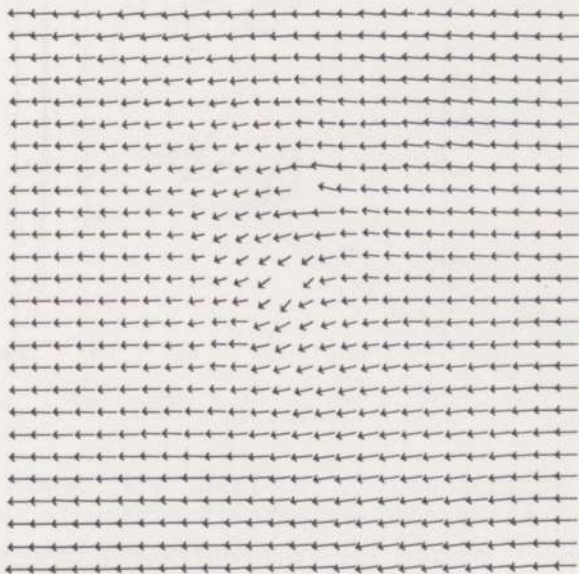


Figure 15. Vector wind field at 4000 m above sea level after 5015 s of model time.

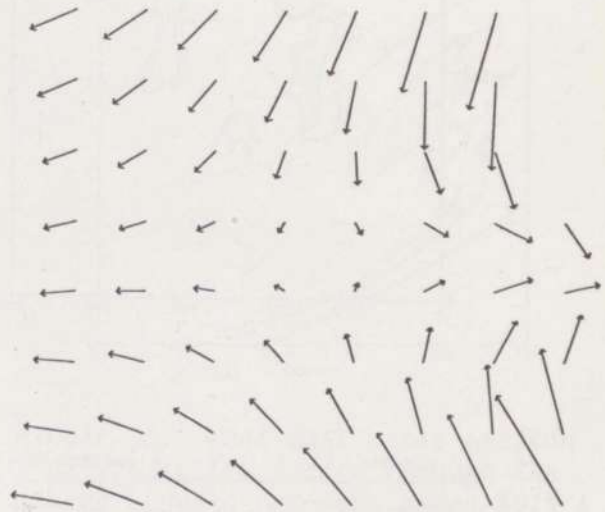
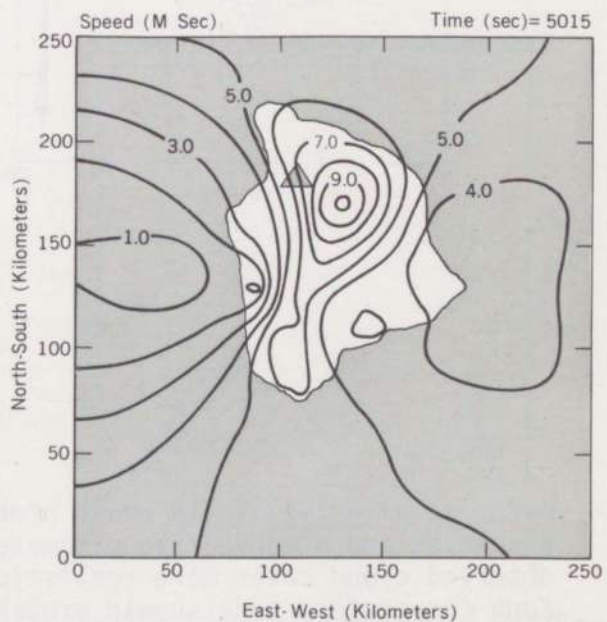
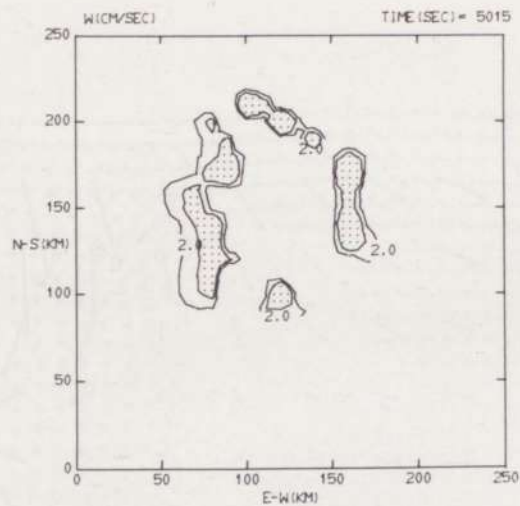


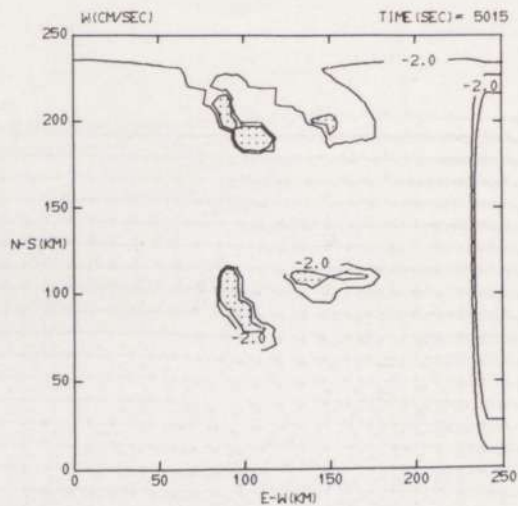
Figure 16. Expanded view of Kona convergence zone corresponding to the shaded area of Fig. 11.

Figure 17. Wind speed at the first grid point above the lower boundary (approximately 18 m) after 5015 s of model time. The triangle indicates the approximate location of Plate 2.

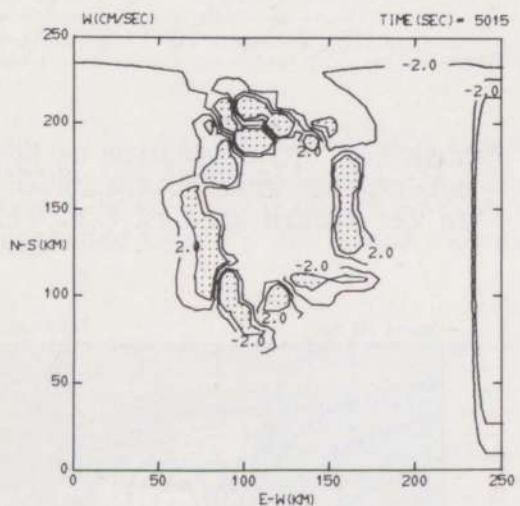




a.



b.



c.

Figure 18. a. Positive vertical velocity field 1000 m above sea level after 5015 s of model time. Shaded areas indicate values in excess of 5 cm/s. b. Negative vertical velocity field 1000 m above sea level after 5015 s of model time. Shaded areas indicate sinking motion in excess of 5 cm/s. c. Vertical velocity at 1000 m above sea level after 5015 s of model time.

Mordy et al. (1957). It would probably be necessary to include warm rain processes and a convective parameterization scheme in order to simulate the observed cloud cover more realistically. The lack of any cloud cover in the Kona convergence zone should probably not cause any great surprise in view of the model's neglect of cumulus processes. The calculated North Kohala cloud (Figs. 22-23), on the other hand, appears deeper than the saddle cloud and may be representative of the actual Kohala cloud (Plate 3).

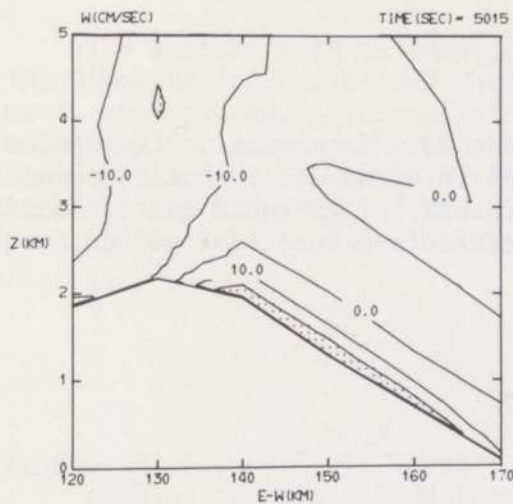


Figure 19. West-east cross section of vertical velocity through the saddle cloud after 5015 s of model time. Shaded areas indicate values in excess of 20 cm/s.

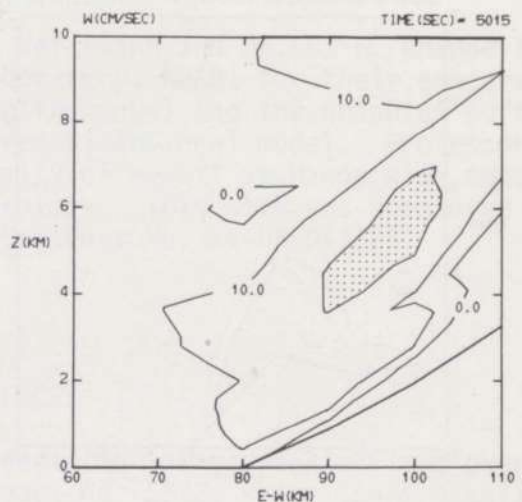


Figure 20. West-east cross section of vertical velocity through the Kona convergence zone after 5015 s of model time. Shaded areas indicate values in excess of 20 cm/s.

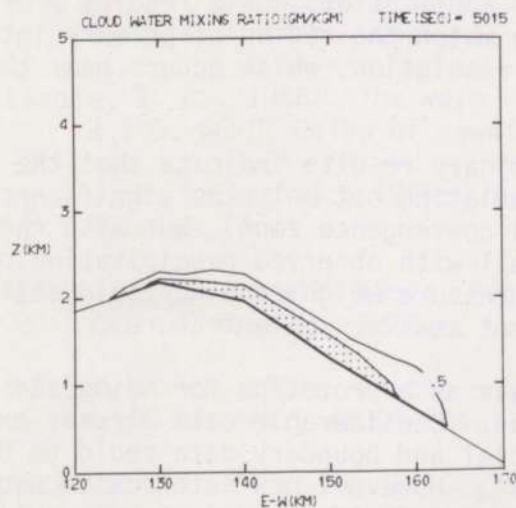


Figure 21. Cloud water mixing ratio through the saddle cloud corresponding to the same cross section as Fig. 19. Shaded areas indicate values in excess of 1 gm/kgm.

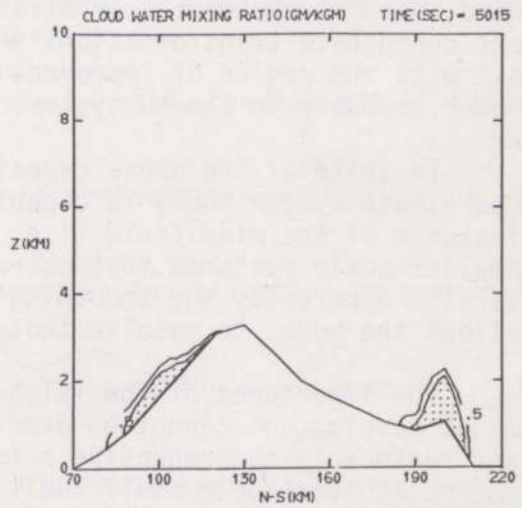


Figure 22. North-south cross section of cloud water showing a portion of the Kohala cloud after 5015 s of model time. Shaded areas indicate values in excess of 1 gm/kgm.

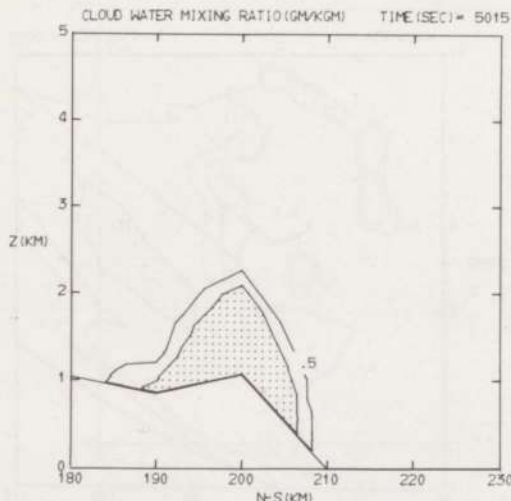


Figure 23. An expanded view of the Kohala cloud cross section shown in Fig. 22. The shaded area indicates values in excess of 1 gm/kgm.

14. CONCLUSION

Terrain-following coordinate systems, such as the one used in the present calculations, eliminate the need for special boundary treatments where quasi-horizontal computational surfaces intersect the surface topography. However, one seldom gets something for nothing. In the case of a non-uniformly spaced terrain-following system, the modeler must contend with variable vertical resolution. The vertical resolution shown in Table 1 is probably sufficient for most applications in the lower troposphere. On the other hand, upper tropospheric or stratospheric applications would require a different coordinate transformation in order to match the region of primary interest with the region of improved vertical resolution, which occurs near the lower boundary in the Nu system.

In spite of the above caveat, preliminary results indicate that the Nu coordinate system model is capable of simulating not only the significant features of the wind field (i.e. the Kona convergence zone), but also the smaller scale features that correspond well with observed precipitation patterns. Apparently the smoothing of the pressure weighted wind field still allows the model to resolve those important smaller scale features.

The importance of the island of Hawaii as a prototype for mesoscale model development cannot be overemphasized. Considerable data already exist, and reasonably comprehensive sets of initial and boundary data could be obtained at relatively small additional cost. However, new interactive programs combining numerical modeling studies and field investigations would derive considerable benefit from the remote sensing capabilities of aircraft and satellites (see Plates 1 and 4). Comprehensive studies of the spatially varying but semi-permanent wind, cloud, and precipitation regimes of Hawaii would (1) assist in the evaluation of mesoscale models, and (2) provide the physical insight required for improved parameterization of sub-grid scale transport processes.

15. ACKNOWLEDGMENTS

The authors wish to thank Dr. H. K. Weickmann and Dr. C. F. Chappell of the Atmospheric Physics and Chemistry Laboratory, NOAA, for their encouragement, support, and guidance in developing the model and the graphics software necessary for viewing the output of a three-dimensional model. Professors T. Schroeder and C. S. Ramage of the University of Hawaii at Manoa also contributed to our knowledge of Hawaiian meteorology. This work was sponsored in part by the Bureau of Reclamation under Contract No. 14-06-D-7676.

16. REFERENCES

- Anthes, R. A. and T. T. Warner, 1974: Prediction of mesoscale flows over complex terrain. ECOM Technical Report No. 5532, White Sands Missile Range, New Mexico 88002.
- Arakawa, A. and Y. Mintz, 1974: The UCLA general circulation model. Notes distributed at the workshop, 25 March-4 April 1974, Dept. of Meteorology, UCLA.
- Chopra, K. P., 1973: Atmospheric and oceanic flow problems introduced by islands. *Advances in Geophysics*, 16:297-421.
- De Rivas, E. K., 1972: On the use of nonuniform grids in finite difference equations. *J. Comp. Phys.*, 10:202-210.
- Fiedler, F., and H. Panofsky, 1970: Atmospheric scales and spectral gaps. *Bull. Am. Meteor. Soc.*, 51:1114-1119.
- Lavoie, R. L., 1966: The warm rain project in Hilo, Hawaii, summer 1965. H.I.G.-66-5, Univ. of Hawaii.
- Lavoie, R. L., et al., 1967: The warm rain project in Hawaii. *Tellus*, 19: 347-461.
- Mordy, W. A., et al., 1957: Project Shower, an investigation on warm rainfall in Hawaii. *Tellus*, 9:471-590.
- Murray, F. W., 1967: On the computation of saturation vapor pressure. *J. Appl. Meteor.*, 6:203-204.
- Nickerson, E. C. and V. E. Smiley, 1975: Surface layer and energy budget parameterizations for mesoscale models. *J. Appl. Meteor.*, 14:297-300.
- NOAA, 1972: Local climatological data; annual summary...; Hilo, Hawaii. U.S. Dept. of Commerce, National Oceanic and Atmospheric Administration, Environmental Data Service.

- O'Brien, J., 1970: On the vertical structure of the eddy exchange coefficient in the planetary boundary layer. *J. Atmos. Sci.*, 27:1213-1215.
- Patzert, W. C. , 1970: Eddies in Hawaiian waters. H.I.G.-69-8, University of Hawaii.
- Priestley, C. H. B., 1959: *Turbulent Transfer in the Lower Atmosphere*. Univ. of Chicago Press, Chicago, Ill.
- Sellers, W. D., 1966: *Physical Climatology*. Univ. of Chicago Press, Chicago, Ill.
- Shapiro, R., 1970: Smoothing, filtering and boundary effects. *Rev. Geophys. Space Phys.*, 8:359-387.
- Sutton, O. G., 1953: *Micrometeorology*, McGraw-Hill, New York.
- Webb, E. K., 1970: Profile relationships: The log-linear range and extension to strong stability. *Q. J. Roy. Meteor. Soc.*, 96:67-90.
- Weiss, C. E., and J. F. Purdom, 1974: The effect of early-morning cloudiness on squall line activity. *Mon. Wea. Rev.*, 102:400-402.

APPENDIX A.

BASIC NOMENCLATURE

A^n	Unspecified variable at time level n	e_s	Saturation vapor pressure with respect to water
C_p	Specific heat at constant pressure	f	Coriolis parameter [= 5×10^{-5}]
F	Normalized surface layer wind speed	g	Acceleration of gravity [= 9.8062]
F_S	Friction term in the entropy equation	h	Height of the first grid point above the lower boundary
F_U	Friction term in the x equation of motion	i, j, k	Grid locations in the (x, y, v) coordinate system
F_V	Friction term in the y equation of motion	k	Von Karman constant [= .35]
F_W	Fraction term in the moisture equation	q_{cw}	Cloud water mixing ratio
G	Normalized surface layer heat flux	q_h	Water vapor mixing ratio at $z=h$
$K(u)$	Exchange coefficient for momentum	q_o	Water vapor mixing ratio at $z=z_0$
$K(T)$	Exchange coefficient for thermodynamic variables	q_v	Water vapor mixing ratio
L	Monin-Obukhov length $\left[= - \frac{u_*^3 h}{kg w'^{\theta_0}} \right]$	q_{vs}	Saturated mixing ratio
L	Latent heat of vaporization	t	Time
P	Pressure	u	Velocity component in the x direction
\hat{P}	Normalized pressure $\left[= \left(\frac{P}{P_0} \right)^K \right]$	u_*	Friction velocity
P_0	Reference pressure	u_h	Wind speed at $z = h$
P_s	Pressure at the ground ($v = 1$)	v	Velocity component in the y direction
P_T	Pressure at the top of the atmosphere ($v = 0$)	w	Velocity component in the z direction
Q_e	Moisture flux	x, y	Horizontal coordinates in the Nu coordinate system
Q_s	Sensible heat flux	z	Vertical coordinate
R	Gas constant [= 287.04]	z_A	Height of the planetary boundary layer
R	Boundary layer constant [= .74]	z_B	Height of the surface layer
$R_i B$	Bulk Richardson number	z_0	Surface roughness length
S	Entropy variable [= $\pi(\ln(T/\hat{P}) + Lq_v/C_p T)$]	$w'q_0'$	Surface moisture flux
T	Temperature	α	Surface heat flux
T_s	Temperature corresponding to saturated conditions	β	Surface wind direction [= $\tan^{-1}(v_h/u_h)$]
T_{uns}	Temperature corresponding to unsaturated conditions	γ	Surface layer constant [= 4.7]
T^*	Virtual temperature [= $T(1+0.61 q_v)$]	γ''	Surface layer constant [= 15]
U	Pressure weighted wind component [= πu]	ζ	Surface layer function [= $(1-\gamma z/L)^{.25}$]
U_h	Pressure weighted wind component at $z=h$	ζ_0	Surface layer function [= $(1-\gamma z_0/L)^{.25}$]
V	Pressure weighted wind component [= πv]	n	Surface layer function [= $(1-\gamma z/L)^{.25}$]
V_h	Pressure weighted wind component at $z=h$	n_0	Surface layer function [= $(1-\gamma z_0/L)^{.25}$]
W	Pressure weighted water mixing ratio [= $\pi(q_v + q_{cw})$]		

θ	Potential temperature [= T/\hat{P}]
θ_h	Potential temperature at $z = h$
θ_0	Potential temperature at $z = z$
κ	Thermodynamic constant [= 2/7]
λ	Dummy variable
v	Transformed vertical coordinate
\dot{v}	Time derivative of v ; $\dot{v} = dv/dt$
π	Pressure variable; $\pi = P_S - P_T$
σ	Vertical coordinate; $\sigma = \sigma(v) = (p-p_T)/\pi$
F	Function
σ'	Vertical derivative of σ ; $\sigma' = d\sigma/dv$
$\dot{\sigma}$	Time derivative of σ ; $\dot{\sigma} = d\sigma/dt$
ϕ	Geopotential; $\phi = gz$
ω	Vertical motion in the P system; $\omega = dp/dt$
Δt	Time step [= 10 sec, except that the last time step was 15 sec]
$\Delta x, \Delta y$	Horizontal grid length [= 10 km]
Δz	Boundary layer thickness $\Delta z = z_A - z_B$
Δv	Vertical grid length [= 1/15]

APPENDIX B. TERRAIN PARAMETERS

A soil parameter and a vegetation parameter have been assigned to each grid point at the lower boundary of the model. The two surface parameters are further subdivided and a number is assigned to each category. Those numbers are then used to estimate the surface roughness length and mixing ratio at the individual grid points.

Table B1. Soil Parameters

Soil Type	Coded Form
Sea	1
Dry	2
Semimoist	3
Wet	4
Lava	5
Sand	6

Table B2. Vegetation Parameters

Vegetation Type	Coded Form
None	1
Short Grass	2
Tall Grass	3
Shrub	4
Forest	5

The relative humidity at the surface was set equal to 100% except for soil types 2 and 3, which were assigned the values 80% and 90% respectively.

Table B3. Roughness Parameters

Soil Type	Vegetation Type	Roughness Length (meters)
Sea	None	0.0001
Lava	None	0.01
Dry	Grass	0.01
Dry	Shrub	0.2
Semimoist	Grass	0.05
Semimoist	Shrub	0.5
Wet	Grass	0.1
Wet	Shrub	1.0
Wet	Forest	3.0

All points on the 26 by 26 not listed below are over water. Their surface parameters are coded (0,1,1), where the first digit represent height above sea level in meters, the second the soil parameter, and the third the vegetation parameter.

Table B4. Terrain Heights and Surface Parameters for Hawaii

I	J	Z	S	V	I	J	Z	S	V
12	8	1	6	1	10	16	1510	4	4
11	9	60	5	1	11	16	1580	3	3
12	9	340	5	1	12	16	1940	5	1
10	10	240	5	1	13	16	2150	5	1
11	10	700	3	4	14	16	2150	5	1
12	10	840	3	5	15	16	1830	5	1
13	10	430	3	3	16	16	1330	4	5
10	11	550	4	5	17	16	720	4	5
11	11	1650	4	4	18	16	260	4	5
12	11	1580	4	5	19	16	30	4	4
13	11	820	4	5	8	17	20	3	3
14	11	120	4	3	9	17	880	4	4
10	12	670	4	5	10	17	1300	3	3
11	12	2130	5	1	11	17	1340	5	1
12	12	2290	5	1	12	17	1600	5	1
13	12	1860	4	5	13	17	1810	5	1
14	12	700	4	3	14	17	2130	2	4
15	12	590	5	1	15	17	1910	4	4
16	12	210	2	2	16	17	1250	4	5
17	12	30	2	2	17	17	670	4	5
10	13	580	4	5	18	17	60	4	5
11	13	2100	5	1	19	17	20	4	3
12	13	3020	5	1	9	18	150	5	1
13	13	2760	5	1	10	18	500	5	1
14	13	1650	4	5	11	18	900	5	1
15	13	930	4	4	12	18	1310	2	3
16	13	1000	3	4	13	18	2470	2	3
17	13	930	4	4	14	18	3990	5	1
18	13	640	4	4	15	18	2680	3	4
19	13	90	3	4	16	18	1580	4	5
10	14	850	4	5	17	18	820	4	5
11	14	1900	4	4	18	18	90	4	4
12	14	3200	5	1	10	19	90	5	1
13	14	3960	5	1	11	19	430	2	4
14	14	2650	5	1	12	19	1010	2	4
15	14	1650	4	4	13	19	1430	2	4
16	14	1280	4	5	14	19	2190	2	2
17	14	910	4	5	15	19	2130	4	4
18	14	620	4	5	16	19	1370	4	5
19	14	410	4	5	17	19	520	4	5
20	14	170	4	5	11	20	400	2	2
9	15	30	2	2	12	20	820	2	2
10	15	1160	4	4	13	20	1010	3	4
11	15	1740	5	1	14	20	1110	4	4
12	15	2600	5	1	15	20	850	4	5
13	15	3230	5	1	16	20	380	4	5
14	15	3020	5	1	10	21	110	2	2
15	15	2270	5	1	11	21	1070	3	4
16	15	1490	4	5	12	21	1040	4	5
17	15	880	4	5	13	21	580	4	5
18	15	430	4	4	14	21	270	4	5
19	15	170	4	4	10	22	340	3	3
20	15	80	4	4	11	22	590	4	5
9	16	370	4	4	12	22	1	4	4
					10	23	3		3

APPENDIX C. EXCERPT FROM U.S.W.B. CLIMATOLOGICAL SUMMARY (NOAA, 1972)

The city of Hilo is located near the midpoint of the eastern shore of the Island of Hawaii. This island is by far the largest of the Hawaiian group, with an area of 4,038 square miles, more than twice that of all the other islands combined. Its topography is dominated by the great volcanic masses of Mauna Loa and Mauna Kea, both of which exceed 13,600 feet in elevation, and of Hualalai (8,271 feet), the Kohala Mountains (5,480 feet), and Kilauea (4,090 feet). In fact the island consists entirely of the slopes of these mountains and of the broad saddles between them.

Hawaii is diamond-shaped, about 93 miles long, from north to south, and 76 miles wide. Its highest point is the summit of Mauna Kea at 13,796 feet. Mauna Loa and Kilauea, which occupy the southern half of the island, are still active volcanoes and hence smooth-sloped, in contrast to the deeply eroded valleys that indent portions of Mauna Kea and the Kohala Mountains.

Hawaii lies well within the belt of northeasterly trade winds generated by the semi-permanent Pacific high pressure cell to the north and east. The climate of the island is greatly influenced by terrain. Its outstanding features are the marked variations in rainfall with elevation and from place to place, the persistent northeasterly trade winds in areas exposed to them, and the equable temperatures from day to day and season to season in localities near sea level.

Over the island's windward slopes, rainfall occurs principally in the form of showers within the ascending moist trade winds. Mean annual rainfall increases from 100 inches or more along the coasts to a maximum of over 300 inches at elevations of 2,000 to 3,000 feet, and then declines to about 15 inches at the summits of Mauna Kea and Mauna Loa. In general, leeward (southern and western) areas are topographically sheltered from the trades — hence from trade-wind showers — and are therefore drier; although sea breezes created by daytime heating of the land move onshore and upslope, causing afternoon and evening cloudiness and showers. Where mountain slopes are steeper, mean annual rainfall may range from 30 inches along the coast to 120 inches at elevations of 2,500 to 3,000 feet. The driest locality on the island — and in the State — with an average annual rainfall of less than 10 inches, is the coastal strip just leeward of the southern portion of the Kohala Mountains and of the saddle between the Kohalas and Mauna Kea.

These marked contrasts in rainfall are reflected in soil and vegetation, with frequent abrupt transitions from lush tropical growth to near-desert conditions, such as occurs between Kilauea's wet windward slopes and the Kau Desert just to the south.

Within the city of Hilo itself, average rainfall varies from about 130 inches a year near the shore to as much as 200 inches in mountain sections. The wettest part of the island, with a mean annual rainfall exceeding 300 inches, lies about 6 miles upslope from the city limits. Rain falls on about 280 days a year in the Hilo area.

Hawaii's equable temperatures are associated with its mid-ocean location and the small seasonal variation in the amount of energy received from the sun. At Hilo, the range in average temperature from February and March, the coldest months, to August, the warmest, is only 5.2° F and the average daily range, 15.1° F. The highest temperature of record at Hilo Airport is 94° F; the lowest 53° F. Greater variations occur in localities with less rain and cloud, but temperatures in the mid-90's and low 50's are uncommon anywhere on the island near sea level.

The trade winds prevail throughout the year (although they may be absent for days or even weeks at a time) and profoundly influence the climate. However, the island's entire western coast is sheltered from the trades by high mountains, except that unusually strong trade winds may sweep through the relatively low (2,600-foot) saddle between the Kohala Mountains and Mauna Kea and reach the areas to the lee. But even places exposed to the trades may be affected by local mountain circulations. For example, the prevailing wind at Hilo Airport is not the northeasterly trade, but the southwesterly wind that drifts downslope off Mauna Loa during the night and early morning hours.

Except for heavy rain, really bad weather seldom occurs. Thunderstorms average only 8 per year, and are rarely severe. During the winter, cold fronts or the cyclonic storms of subtropical origin (the so-called Kona storms) may bring blizzards to the upper slopes of Mauna Loa and Mauna Kea, with snow extending at times to 9,000 feet or below and icing nearer the summit.

Storms crossing the Pacific a thousand miles to the north, or Kona storms closer by, may generate seas that cause heavy swell and surf along the northern, eastern, and southwestern shores of the island.

ERRATUM

NOAA Technical Report ERL 377-APCL 39

A Three-Dimensional Simulation of Winds and Non-Precipitating Orographic Clouds Over Hawaii

Everett C. Nickerson and Elemer L. Magaziner

September 1976

U.S. Department of Commerce
National Oceanic and Atmospheric Administration
Environmental Research Laboratories

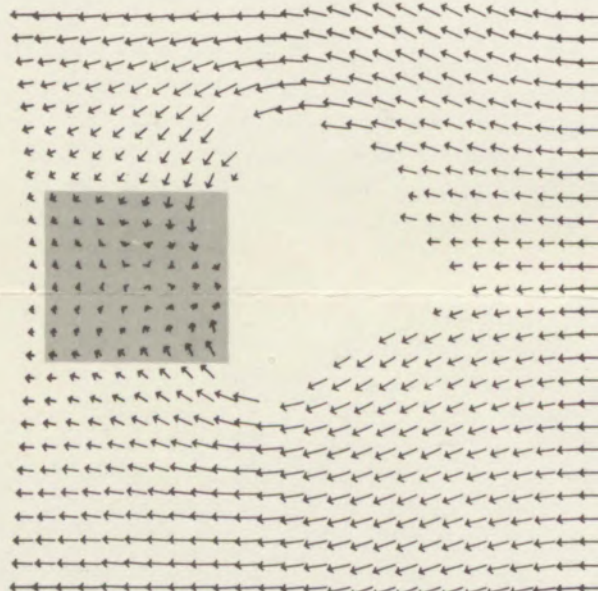


Figure 11. p. 22

Environmental Research LABORATORIES

The mission of the Environmental Research Laboratories (ERL) is to conduct an integrated program of fundamental research, related technology development, and services to improve understanding and prediction of the geophysical environment comprising the oceans and inland waters, the lower and upper atmosphere, the space environment, and the Earth. The following participate in the ERL missions:

MESA	<i>Marine EcoSystems Analysis Program.</i> Plans, directs, and coordinates the regional projects of NOAA and other federal agencies to assess the effect of ocean dumping, municipal and industrial waste discharge, deep ocean mining, and similar activities on marine ecosystems.	GFDL	<i>Geophysical Fluid Dynamics Laboratory.</i> Studies the dynamics of geophysical fluid systems (the atmosphere, the hydrosphere, and the cryosphere) through theoretical analysis and numerical simulation using powerful, high-speed digital computers.
OCSEA	<i>Outer Continental Shelf Environmental Assessment Program.</i> Plans, directs, and coordinates research of federal, state, and private institutions to assess the primary environmental impact of developing petroleum and other energy resources along the outer continental shelf of the United States.	APCL	<i>Atmospheric Physics and Chemistry Laboratory.</i> Studies cloud and precipitation physics, chemical and particulate composition of the atmosphere, atmospheric electricity, and atmospheric heat transfer, with focus on developing methods of beneficial weather modification.
WM	<i>Weather Modification Program Office.</i> Plans, directs, and coordinates research within ERL relating to precipitation enhancement and mitigation of severe storms. Its National Hurricane and Experimental Meteorology Laboratory (NHEML) studies hurricane and tropical cumulus systems to experiment with methods for their beneficial modification and to develop techniques for better forecasting of tropical weather. The Research Facilities Center (RFC) maintains and operates aircraft and aircraft instrumentation for research programs of ERL and other government agencies.	NSSL	<i>National Severe Storms Laboratory.</i> Studies severe-storm circulation and dynamics, and develops techniques to detect and predict tornadoes, thunderstorms, and squall lines.
AOML	<i>Atlantic Oceanographic and Meteorological Laboratories.</i> Studies the physical, chemical, and geological characteristics and processes of the ocean waters, the sea floor, and the atmosphere above the ocean.	WPL	<i>Wave Propagation Laboratory.</i> Studies the propagation of sound waves and electromagnetic waves at millimeter, infrared, and optical frequencies to develop new methods for remote measuring of the geophysical environment.
PMEL	<i>Pacific Marine Environmental Laboratory.</i> Monitors and predicts the physical and biological effects of man's activities on Pacific Coast estuarine, coastal, deep-ocean, and near-shore marine environments.	ARL	<i>Air Resources Laboratories.</i> Studies the diffusion, transport, and dissipation of atmospheric pollutants; develops methods of predicting and controlling atmospheric pollution; monitors the global physical environment to detect climatic change.
GLERL	<i>Great Lakes Environmental Research Laboratory.</i> Studies hydrology, waves, currents, lake levels, biological and chemical processes, and lake-air interaction in the Great Lakes and their watersheds; forecasts lake ice conditions.	AL	<i>Aeronomy Laboratory.</i> Studies the physical and chemical processes of the stratosphere, ionosphere, and exosphere of the Earth and other planets, and their effect on high-altitude meteorological phenomena.
		SEL	<i>Space Environment Laboratory.</i> Studies solar-terrestrial physics (interplanetary, magnetospheric, and ionospheric); develops techniques for forecasting solar disturbances; provides real-time monitoring and forecasting of the space environment.